catalysts

MDPI

*Article*

# Effects of the Acidic and Textural Properties of Y-Type Zeolites on the Synthesis of Pyridine and 3-Picoline from Acrolein and Ammonia

**Israel Pala-Rosas [1], José Luis Contreras [2,*], José Salmones [1], Ricardo López-Medina [2], Deyanira Angeles-Beltrán [3], Beatriz Zeifert [4], Juan Navarrete-Bolaños [5] and Naomi N. González-Hernández [2]**

[1] Postgraduate Studies Section, Escuela Superior de Ingeniería Química e Industrias Extractivas, Instituto Politécnico Nacional, Av. Instituto Politécnico Nacional s/n, Col. Nueva Industrial Vallejo, Mexico City 07738, Mexico
[2] Energy Departament, Universidad Autónoma Metropolitana-Azcapotzalco, Av. San Pablo 180, Col. Reynosa, Mexico City 02200, Mexico
[3] Basic Sciences Departament, Universidad Autónoma Metropolitana-Azcapotzalco, Av. San Pablo 180, Col. Reynosa, Mexico City 02200, Mexico
[4] Department of Engineering in Metallurgy and Materials, Escuela Superior de Ingeniería Química e Industrias Extractivas, Instituto Politécnico Nacional, Av. Instituto Politécnico Nacional s/n Col. Nueva Industrial Vallejo, Mexico City 07738, Mexico
[5] Instituto Mexicano del Petróleo, Eje Central Lázaro Cárdenas 152, Col. San Bartolo Atepehuacán, Mexico City 07730, Mexico
* Correspondence: jlcl@azc.uam.mx; Tel.: +52-55-91911047

**Abstract:** A set of Y-type zeolites with Si/Al atomic ratios between 7–45 were studied as catalysts in the aminocyclization reaction between acrolein and ammonia to produce pyridine and 3-picoline. The catalytic activity tests at 360 °C revealed that the acrolein conversion increased in the order Z45 < ZY34 < ZY7 < ZY17, in agreement with the increase of the total acidity per gram of catalyst. In all cases, pyridine bases and cracking products (acetaldehyde and formaldehyde) were detected in the outflow from the reactor. The total yield of pyridines was inversely proportional to the total acidity for the catalysts, which presented large surface areas and micro- and mesoporosity. The selectivity towards 3-picoline was favored when using catalysts with a Brønsted/Lewis acid sites ratio close to 1. The formation of pyridine occurred more selectively over Lewis acid sites than Brønsted acid sites. The deactivation tests showed that the time on stream of the catalysts depended on the textural properties of zeolites, i.e., large pore volume and large BET area, as evidenced by the deactivation rate constants and the characterization of the spent catalysts. The physicochemical properties of the catalysts were determined by XRD, UV-vis, and Raman spectroscopies, infrared spectroscopy with adsorbed pyridine, $N_2$ physisorption, and SEM-EDXS. After the reaction, the spent catalysts were characterized by XRD, Raman spectroscopy, TGA, and SEM-EDXS, indicating that the uniform deposition of polyaromatic species on the catalyst surface and within the porous system resulted in the loss of activity.

**Keywords:** acrolein aminocyclization; pyridine; 3-picoline; Y zeolite; Brønsted/Lewis acid sites; micro/mesoporous zeolites; catalyst deactivation



**Citation:** Pala-Rosas, I.; Contreras, J.L.; Salmones, J.; López-Medina, R.; Angeles-Beltrán, D.; Zeifert, B.; Navarrete-Bolaños, J.; González-Hernández, N.N. Effects of the Acidic and Textural Properties of Y-Type Zeolites on the Synthesis of Pyridine and 3-Picoline from Acrolein and Ammonia. *Catalysts* **2023**, *13*, 652. https://doi.org/10.3390/catal13040652

Academic Editors: Maja Milojević-Rakić and Danica Bajuk-Bogdanović

Received: 21 January 2023
Revised: 20 March 2023
Accepted: 22 March 2023
Published: 26 March 2023



## 1. Introduction

Pyridine bases are compounds of interest in several areas of industry and technology, with pyridine (azobenzene) and the series of picolines (methylpyridines) being the most important [1,2]. Due to their cyclic structure which is deficient π-type electrons and contains a basic nitrogen atom in the ring, and the methyl group attached to the ring in the case of picolines, pyridine compounds present unique physical and chemical properties such as weak basicity, dipolar and aprotic character, higher boiling point than benzene, miscibility with water and organic solvents, as well as reactions at the ring atoms and reactions at

the substituents attached to the ring. Thus, pyridine bases are widely used as solvents in organic reactions and as precursors of drugs, polymers, insecticides, herbicides, dyes, adhesives, and explosives, or as denaturalizing agents of ethanol and antifreeze [3,4].

The great demand for pyridine compounds caused by the generation of new products has led to the development of different synthesis methods so that, during the last decades, the production of pyridines from several raw materials has been investigated, namely alcohols, aldehydes, ketones, dicarbonyl compounds, dicianoalkanes, alkenes, and alkynes, either in the presence of ammonia ($NH_3$) or amines. However, the most employed process has been the aminocyclization of aldehydes with $NH_3$ [2–6]. The reaction was first studied by Tschitschibabin [7], using alumina ($Al_2O_3$) as a catalyst for the reaction between $NH_3$ and different aldehydes at temperatures between 300 °C and 400 °C, obtaining pyridine and several mono- and polyalkyl substituted pyridines.

Currently, industrial production of pyridine is performed by the gas-phase reaction between $NH_3$ and a mixture of formaldehyde and acetaldehyde in the presence of a ZSM-5 catalyst. This process yields 3-picoline (3-methylpyridine) as the main byproduct and depending on the acetaldehyde/formaldehyde molar ratio in the feedstock, variable amounts of 2-picoline (2-methylpyridine) and 4-picoline (4-methylpyridine) are obtained [2]. Nevertheless, the interest in controlling the selectivity of pyridine products has led to research on the use of modified ZSM-5 catalysts and different raw materials.

Sato et al. [8] compared the catalytic activity of a silica-alumina catalyst ($SiO_2$-$Al_2O_3$) and different protonated zeolites, namely H-A, H-X, H-Y, H-mordenite, H-ZSM-5, and H-ZSM-11, in the gas-phase aminocyclization reaction between formaldehyde and acetaldehyde at 450 °C and atmospheric pressure. In all cases, pyridine was the main reaction product, while 2-, 3- and 4-picoline were obtained in yields around 6%, 6–14%, and 4–8%, respectively, depending on the catalyst. The H-ZSM-5 zeolite showed the best results with 61% of total pyridine yield, 42% of pyridine, 3% of 2-picoline, 11% of 3-picoline, and 5% of 4-picoline. However, a high amount of acid sites promoted coke formation and the rapid deactivation of the catalysts, so a medium acidity exhibited satisfactory results.

The importance of surface acidity in the reaction between formaldehyde, acetaldehyde, and $NH_3$ has been explored with a set of H-ZSM-5 zeolites, with Si/Al ratios of 40, 90, 150, and 240 in a continuous flow reactor at atmospheric pressure and 375 °C [9]. It was found that the increase of the Si/Al ratio, from 40 to 240, resulted in a decrease in the amount of acid sites and thus a decrease in the conversion from 98% to 58%. Additionally, the pyridine selectivity increased from 57% to 76%, and the selectivities to 2- and 3-picoline decreased from 15% to 2% and from 24% to 17%, respectively.

Additionally, the use of oxygenated unsaturated compounds, such as allyl alcohol, crotonaldehyde, acrolein, and acrolein dialkyl acetals, to produce pyridine bases has been reported [5,10–12]. Zhang et al. [10] reported the synthesis of pyridine and 3-picoline by the aminocyclization between acrolein and $NH_3$ in the presence of a ZSM-5 zeolite treated with HF, impregnated with Mg or subjected to both treatments. The best results were obtained using the catalyst sequentially modified (HF/Mg-ZSM-5) in the reaction at 425 °C, reaching pyridine and 3-picoline yields of 27% and 30%, respectively. Compared with the non-treated zeolite, the HF/Mg-ZSM-5 catalyst exhibited less concentration and weaker acid sites. Additionally, the modification of the zeolite resulted in a slight increase in the micro- and mesopore sizes.

The effect of the alkaline- and acid-treatments, and the impregnation with different metals on the catalytic activity of ZSM-5 zeolite in the synthesis of pyridine and 3-picoline from acrolein and acrolein dialkyl acetals, has also been reported [11]. The best results, 61% of the total yield of pyridines, 32% of pyridine yield, and 29% of 3-picoline yield, were obtained with the reaction between acrolein diethyl acetal and ammonia at 450 °C using the zeolite modified with an alkaline-acid treatment and subsequently impregnated with Zn. It was found that the incorporation of Zn changed the acid strength, while the double alkaline-acid treatment originated an increase in the surface area and the mesopore volume.

Similarly, it has been reported that the fluoridation treatment with $NH_4$-HF of an Mg-ZSM-5 zeolite modifies the porosity and acidity of the catalyst as a result of simultaneous desilication and dealumination. These factors improved the total yield of pyridines in the reaction between acrolein dimethyl acetal and $NH_3$ to produce pyridine and 3-picoline. In comparison with the use of the parent zeolite, using the modified catalyst enhanced the 3-picoline yield [12].

The advantage of the use of acrolein in the aminocyclization reaction is that it allows for eliminating the production of 2- and 4-picoline, increasing the selectivity towards pyridine and 3-picoline, also resulting in an easier separation of the reaction products, in comparison with the use of the mixture of acetaldehyde and formaldehyde as feedstock [3].

In addition, intensive research has been conducted recently on the catalytic dehydration of glycerol to produce acrolein over solid acid catalysts. This process represents a sustainable alternative for producing acrolein and its derivatives, in contrast with the prevailing industrial process based on the selective oxidation of petroleum-derived propylene [13–15]. This is because glycerol is obtained as a byproduct during the hydrolysis, saponification, and transesterification processing of vegetable oils and fats, resulting in its high availability and low market price [14,16].

On the other hand, using a zeolite catalyst other than ZSM-5 has been barely reported for synthesizing pyridine compounds. The comparison of H-ZSM-5, H-mordenite, and HY zeolites as catalysts in the reaction between ethanol and $NH_3$ was reported [17]. At 350 °C, the ethanol conversion increased in the order H-ZSM-5 < H-Y < H-mordenite. However, the main difference was reflected in the distribution of reaction products. The main reaction products over the H-ZSM-5 catalyst were ethene (56.9%), pyridine (18%), acetonitrile (4.6%), 2-picoline (3.9%) and $CO_2$ (10.2%), while H-Y and H-mordenite zeolites produced mainly ethene with pyridine selectivities of 1.6% and <0.1%, respectively, without the presence of any other pyridine base.

Grigor'eva et al. [18] studied the reaction between ethanol, formaldehyde, and $NH_3$ using H-ZSM-5, H-ZSM-12, and H-β zeolites as catalysts, obtaining pyridine, picolines, and lutidines as the main reaction products. At 300 °C, the conversion and the pyridine selectivity followed the order H-ZSM-12 < H-ZSM-5 < H-β. The higher conversion obtained with the H-β zeolite was related to the higher concentration of acid sites. The improved pyridine selectivity was associated with the structural characteristics of the catalyst. Furthermore, the H-ZSM-12 and H-ZSM-5 zeolites promoted the formation of 3-picoline, reducing the amounts of 2- and 4-picoline.

It is noticeable that a gap exists in the research and development of catalysts with appropriate physicochemical properties for the synthesis of pyridine bases from aldehydes and ammonia. In this sense, the use of mesoporous or hierarchical zeolites represents a strategy to enhance the reaction performance by improving the transport of reactants and products and the accessibility of reactants to the active sites located inside the pore channels [19–22], which is relevant for reactions in which bulky molecules are involved.

Specifically, the Y zeolite has been widely used for the cyclization of different molecules such as phenol [23], citronellal [24], terpenols [25], unsaturated alcohols [26], and aryl methallyl eters [27]. In synthesizing pyridine bases, the use of the Y-zeolite has been barely reported in the reaction between formaldehyde, acetaldehyde, and ammonia [28] and between acrolein diethyl acetal and ammonia [11].

This study presents the influence of the acidic and textural properties of Y-type zeolites, with Si/Al atomic ratios between 7 and 45, on their catalytic activity during the gas-phase reaction between acrolein and $NH_3$ to produce pyridine and 3-picoline.

## 2. Results and Discussion

### *2.1. Characterization of Catalysts*

The X-ray diffractograms of the Y-type zeolites are presented in Figure 1. All the samples exhibited the typical reflections of the aluminum silicate hydrated with a faujasite-like structure (JCPDS card 00-043-0168) as the unique crystalline phase. The Y zeolites

presented diffraction patterns in agreement with the patterns of ultrastable dealuminated Y zeolites reported in the literature [29].

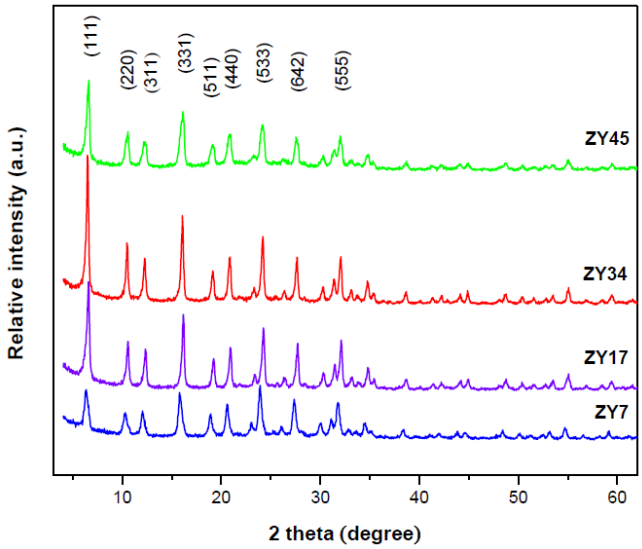


**Figure 1.** X-ray powder diffractograms of the Y-type zeolites.

The average crystal (L) was estimated from the reflection of the plane (331, considering the Scherrer equation. The average crystal sizes were 19.6 nm, 31.4 nm, 31.2 nm, and 16.1 nm for the ZY7, ZY17, ZY34, and ZY45 zeolites, respectively. Similar results were reported for a series of steam-dealuminated Y-zeolites [30].

The UV-vis spectra of the Y-type zeolite samples (Figure 2a) showed a main band between 280 and 285 nm. The decrease of the Al content in the samples produced a reduction of the absorbance. The band is attributed to the charge transfer of the πp-πd transition between oxygen species ($O^{2-}$) and tetrahedral aluminum ($Al^{3+}$) of the zeolite structure [31]. The presence of extra-framework Al cations was evidenced by the extension of the band up to 350 nm, as reported for other zeolite-type solids [31,32].

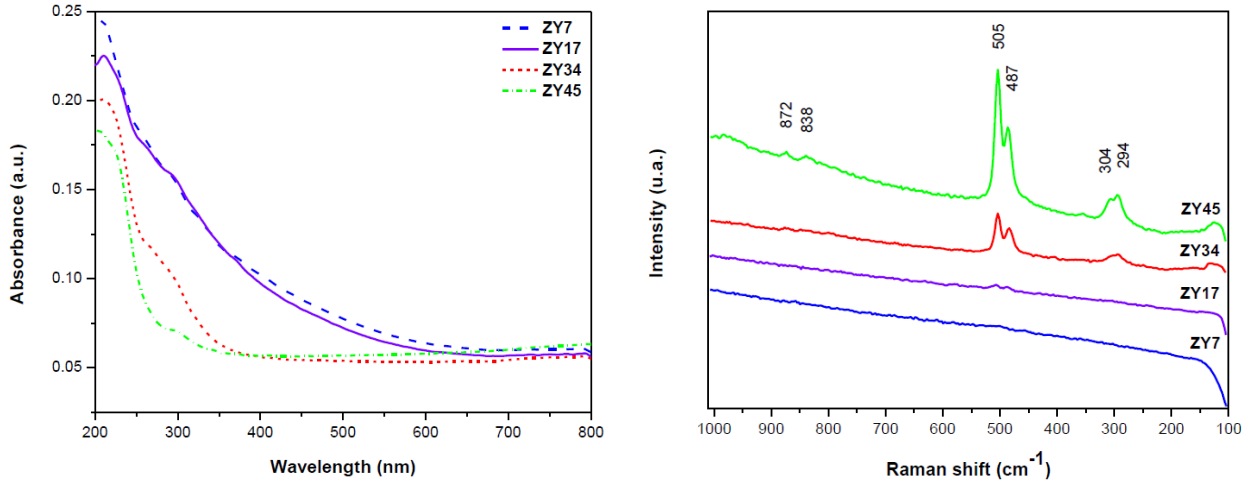


**Figure 2.** (**a**) UV-vis and (**b**) Raman spectra of the Y-type zeolites.

The Raman spectra of the Y-type zeolites are presented in Figure 2b. The zeolite with a Si/Al atomic ratio of 7 did not show bands, while the sample ZY17 displayed barely noticeable bands at 505 $cm^{-1}$ and 487 $cm^{-1}$. Both bands were intense for the ZY34 and ZY45 zeolites, and further bands at 872 $cm^{-1}$, 838 $cm^{-1}$, 304 $cm^{-1}$, and 294 $cm^{-1}$ were also displayed. The bands between 200 $cm^{-1}$ and 400 $cm^{-1}$ are attributed to the low-frequency

torsional modes and the cation-oxygen modes. The strong bands between 300–600 $cm^{-1}$ are associated with the type of rings in the zeolite structure. Y-type zeolites with high silicon contents show bands at approximately 490 $cm^{-1}$ and 500 $cm^{-1}$, attributed to the Si-O-Si bond angles and involving the mixed vibration of stretching and bending of the O atom [33–36]. The bands at 873 $cm^{-1}$ and 839 $cm^{-1}$ were assigned to the displacement of Si atoms bonded to four O atoms, besides the stretch vibrations of the Si-O bonds [37,38].

Figure 3a shows the infrared spectra with adsorbed pyridine (IR-Py) of the zeolite samples at 350 °C. For all samples, the spectra displayed bands at 1450 $cm^{-1}$, 1487 $cm^{-1}$, 1539 $cm^{-1}$, and a broad peak between 1576–1661 $cm^{-1}$. These results agree with the literature, where the bands at 1445–1460 $cm^{-1}$ are reported as a result of the interaction between pyridine and the Lewis acid sites (LAS). The band at 1540 $cm^{-1}$ is related to Brønsted acid sites (BAS) interacting with the pyridine, and the bands between 1485–1489 $cm^{-1}$ are associated with pyridine adsorbed on both Brønsted and Lewis acid sites [39]. The overlapped bands at 1580–1661 $cm^{-1}$ are attributed to ring vibrations of pyridine [40]. Comparing the spectra of the Y zeolites displayed an increment of the absorbance with the rise of the Si/Al ratio from 7 to 17, while a further increase to 34 and 45 resulted in less intense bands, suggesting higher total acidity in the samples with higher aluminum content (Si/Al = 7 and 17) than in the zeolites ZY34 and ZY45.

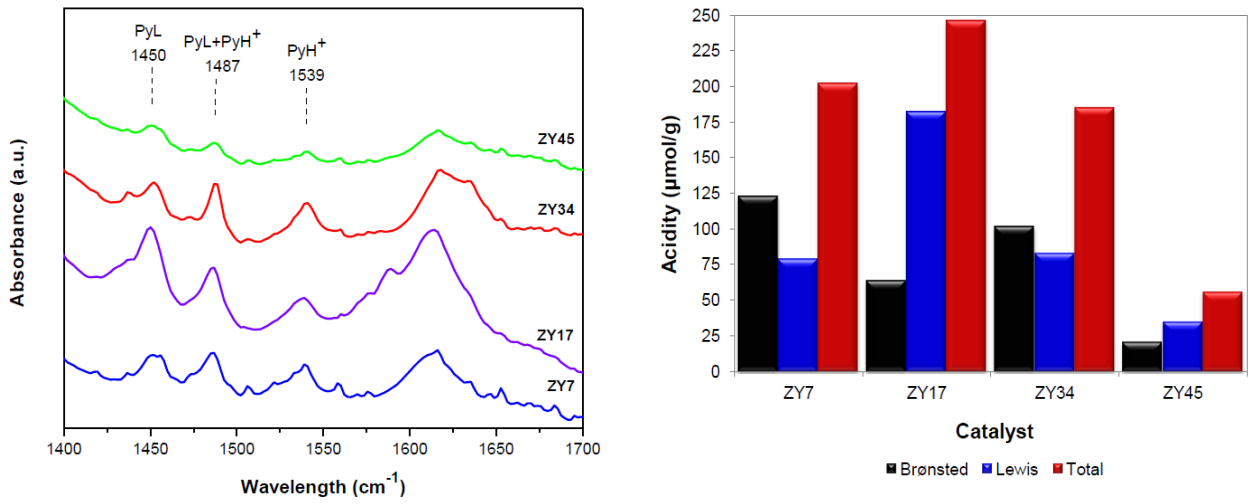


(**a**) (**b**)

**Figure 3.** (**a**) Infrared spectra with adsorbed pyridine, and (**b**) quantification of the Brønsted and Lewis acid sites of the Y-type zeolites at 350 °C.

The quantification of the total, Brønsted and Lewis acidity of the Y-type zeolites at 350 °C is shown in Figure 3b. For the total acidity, the ZY7, ZY17, and ZY34 samples exhibited values of 183–246 µmol Py/g catalyst. The additional increase to an atomic ratio Si/Al = 45 decreased the total acidity, with the lowest value of 56 µmol Py/g catalyst.

The Brønsted acidity exhibited values between 64 and 123 µmol Py/g catalyst for the zeolites with Si/Al atomic ratio between 7 and 34, while the sample ZY45 displayed a value of 21 µmol Py/g catalyst. On the other hand, the Lewis acidity showed values around 79 and 81 µmol Py/g catalyst for the samples ZY7 and ZY34, with maximum and minimum values of 182 and 35 µmol Py/g catalyst for the ZY17 and ZY45 zeolites. As shown by the ratios of the Brønsted and Lewis acidity (BAS/LAS) in Table 1, the Brønsted acidity was predominant in the samples with Si/Al atomic ratios of 7 and 34. The samples ZY17 and ZY45 showed more LAS than BAS, with considerable amounts for the former.

**Table 1.** Physicochemical properties and composition of the Y-type zeolites.

| Catalyst | $L_{(331)}$ [a] | BAS/LAS [b] | Weight Loss [c] (%) | $S_{BET}$ [d] ($m^2/g$) | $V_p$ [e] ($cm^3/g$) | Element (Atom %) [f] | | | Si/Al [g] |
|---|---|---|---|---|---|---|---|---|---|
| | | | | | | Si | Al | O | |
| ZY7 | 19.6 | 1.56 | 16.9 | a | 0.21 | 29.28 | 3.73 | 69.99 | 7.5 |
| ZY17 | 31.4 | 0.35 | 16.1 | 736.0 | 0.25 | 25.39 | 1.66 | 72.95 | 16.1 |
| ZY34 | 31.2 | 1.23 | 10.8 | 749.4 | 0.27 | 30.19 | 0.28 | 69.53 | 36.4 |
| ZY45 | 16.1 | 0.60 | 12.7 | 753.8 | 0.29 | 27.04 | 0.23 | 72.74 | 47.8 |

[a] Average crystal size, [b] ratio of Brønsted/Lewis acid sites at 350 °C, [c] determined by TGA at 350 °C, [d] BET surface area, [e] pore volume, [f] determined by EDXS, [g] determined by AAS.

The thermogravimetric analysis (TGA) in Figure 4a showed a pronounced weight loss of the ZY7 sample from room temperature to 260 °C. For the zeolites ZY17, ZY34, and ZY45 the main weight loss occurs up to 145 °C, 110 °C, and 110 °C, respectively. This weight loss was attributed to eliminating water bound to the zeolite surface, as reported for H-ZSM-5 zeolites [41,42]. The change in weight estimated at 350 °C (close to the reaction temperature) is shown in Table 1, and it is observed that the samples that lost the most water are the ZY7 and ZY17 zeolites, while the ZY34 zeolite lost the less water. This behavior suggests that the samples ZY7 and ZY17 could contain more density of hydroxyl groups (OH) by unit weight when the temperature reached 350 °C, which could be related to the Brønsted or Lewis acidity.

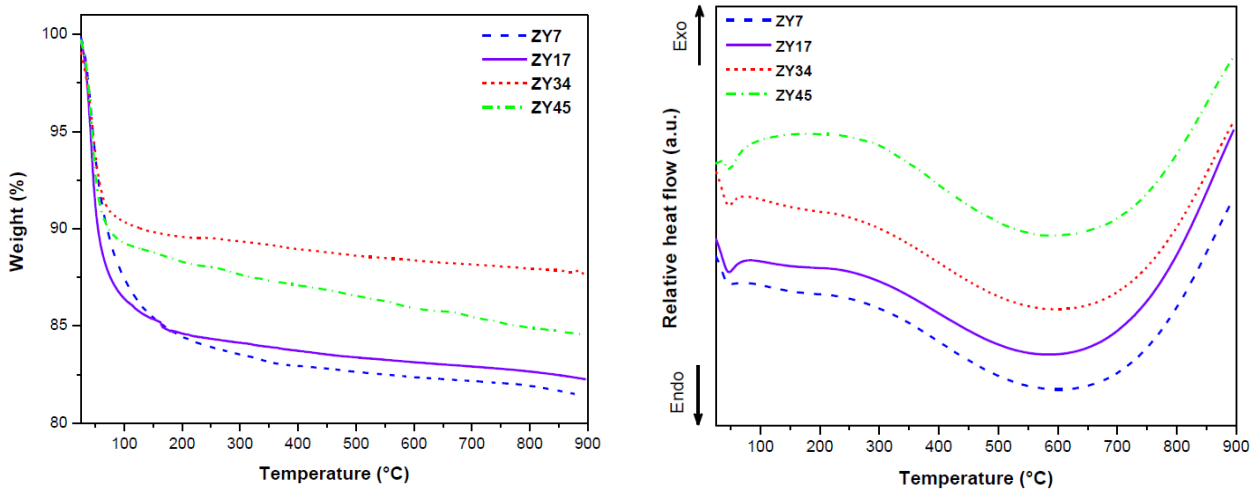


**Figure 4.** (**a**) Thermogravimetric analysis and (**b**) differential thermal analysis of the Y-type zeolites.

The differential thermal analysis (DTA), shown in Figure 4b, exhibited endothermic behavior of the samples at temperatures below 150 °C, typical of a dehydration process, and consistent with the loss of physisorbed water. Further temperature increase resulted in the progressive decrease of heat flow, attributed to the release of OH-groups up to 600 °C.

The $N_2$ isotherms of the Y-type zeolites are presented in Figure 5a. The samples exhibited type IV isotherms and distinctive mesoporous solids. The desorption isotherms presented H4-type hysteresis loops, which are distinguishing agglomerated particles with edges, such as cubes and tetrahedra, resulting in pores with slit shape and uniform size [43,44].

The change of the Si/Al ratio from 7 to 45 increased the specific surface area of the zeolites from 635 to 754 $m^2/g$, as presented in Table 1. For all samples, the main contribution to the surface area was given by the internal area of the porous system of the solids. However, the external area increased when increasing the Si/Al atomic ratio, representing 21%, 28%, 31%, and 35 % of the total area in the order ZY7, ZY17, ZY34, and ZY45.

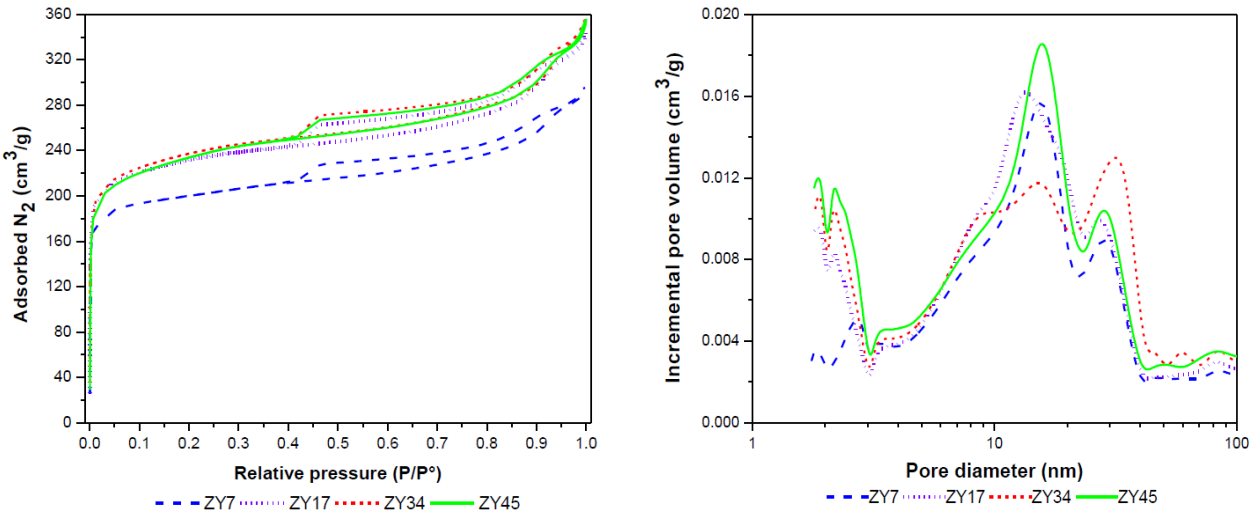


(**a**) (**b**)

**Figure 5.** (**a**) $N_2$ physisorption isotherms, and (**b**) distribution of pore sizes of the Y-type zeolites.

Additionally, the pore volume increased from 0.21 $cm^3$/g to 0.287 $cm^3$/g with the increment in the Si/Al ratio from 7 to 45 (Table 1). The samples showed a proportion of micropores and small mesopores (2–3 nm) besides a mesoporous system with pore sizes between 5 nm and 40 nm.

The scanning electron micrographs (SEM) of the Y-type zeolites are shown in Figure 6. All the samples displayed grains with shapes of the variable and faceted pyramid and hexagonal prisms, which are typical of the Y zeolite [45,46]. Furthermore, the surface of the zeolites was rough, porous, and slightly cracked. The average grain size of the zeolites in this study was 400 nm and did not change significantly with the Si/Al atomic ratio variation. The values correspond approximately with those reported by Taufiqurrahmi et al. [47] of 500 nm for a commercial Y zeolite.

According to the EDXS analysis, the samples are constituted by Si, Al, and O, and the diminishing of the Al content with the increase of the Si/Al atomic ratio was confirmed, as presented in Table 1. The bulk Si/Al atomic ratios of the samples were confirmed by atomic absorption spectroscopy (AAS).

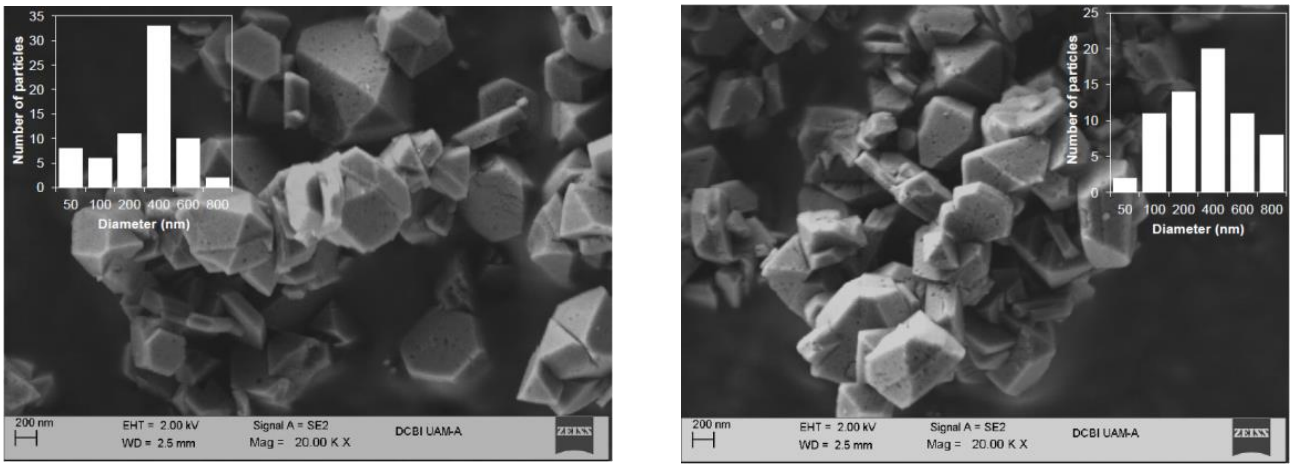


(**a**) (**b**)

**Figure 6.** *Cont.*

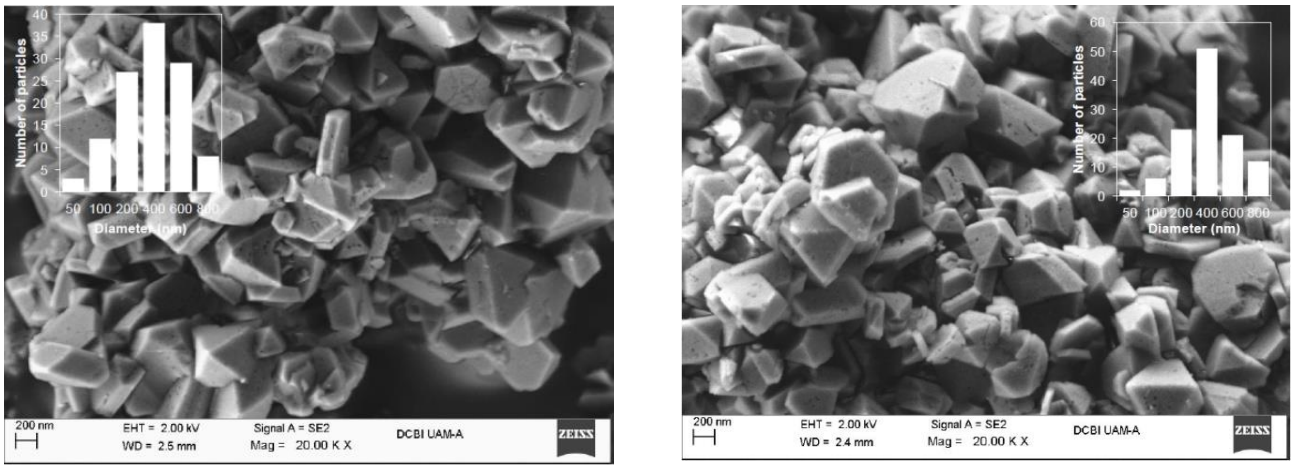


(**c**) (**d**)

**Figure 6.** Scanning electron micrographs and particle size distributions of the zeolites (**a**) ZY7, (**b**) ZY17, (**c**) ZY34, and (**d**) ZY45.

### *2.2. Catalytic Activity*

The Y-type zeolites with different Si/Al atomic ratios were active as catalysts in the reaction between acrolein and ammonia at 360 °C. At this point, it is noteworthy to mention that the reaction conditions (T = 360 °C, GHSV = 4994 $h^{-1}$, molar ratio $NH_3$/acrolein = 2, and pure acrolein vapor feed) were chosen to evaluate the catalytic performance of the zeolites in terms of their acidic and textural properties, minimizing the effects of the process variables on the reaction.

As presented in Figure 7a, The Y-type zeolites achieved almost total conversion of acrolein at the beginning of the process. The acrolein conversion increased in the order ZY45 < ZY34 < ZY7 < ZY17, similar to the total acidity of the catalysts (Figure 3b).

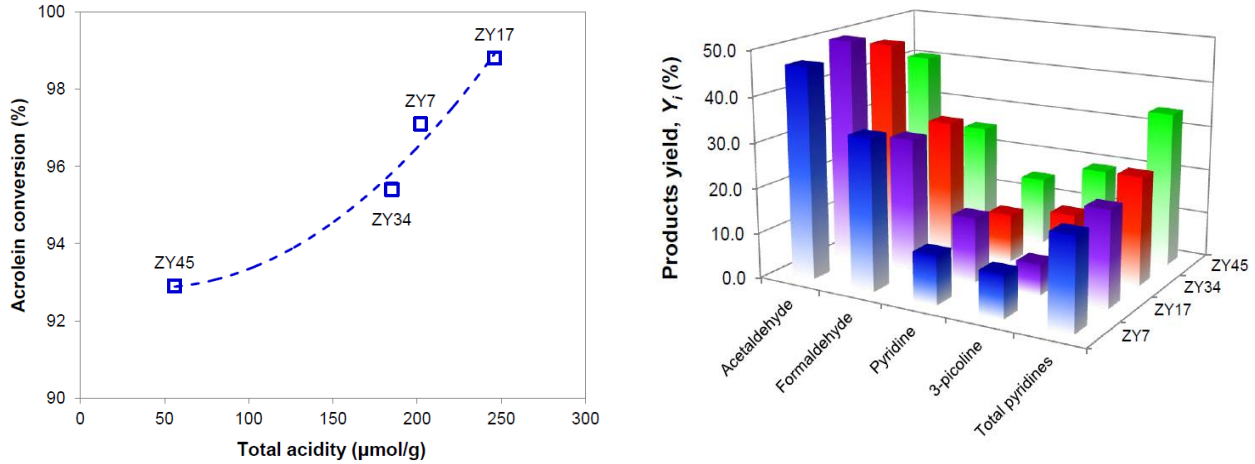


(**a**) (**b**)

**Figure 7.** (**a**) Initial acrolein conversion and, (**b**) initial products yield of the reaction between acrolein and ammonia over the Y-type zeolites. The total yield of pyridine bases = (pyridine + 3-picoline). Reaction conditions: T = 360 °C, molar ratio $NH_3$/acrolein = 2, GHSV = 4994 $h^{-1}$, TOS = 5 min.

The compounds identified at the output stream from the reactor were acetaldehyde, formaldehyde, pyridine, and 3-picoline. For all the catalysts, acetaldehyde was the major reaction product (Figure 7b), which is in agreement with the literature where acetaldehyde is reported as a cracking product of acrolein over acid catalysts [48,49]. The total yield of pyridine bases (pyridine + 3-picoline) improved from 20.2% to 34.2% with the change of the

Si/Al atomic ratio from 7 to 45. Pyridine was produced with yields of 10.7%, 14.3%, 13.2%, and 15% with the ZY7, ZY17, ZY34, and ZY45 zeolites, respectively. 3-picoline achieved yields of around 9.5%, 6.7%, 13.2%, and 19.1% in the same order. These low yields can be attributed to the low reaction temperature, and low $NH_3$/acrolein molar ratio in the feed since it is known [9–12,50–53] that the increase of both variables improves the formation of pyridine compounds and typical reaction conditions for the synthesis of pyridines from aldehydes and ammonia are T = 400–475 °C, $NH_3$/acrolein molar ratios between 4 and 6, as well as the reactant diluted with water.

It is noticeable that the total yield of pyridine bases followed the order ZY7 < ZY17 < ZY34 << ZY45, following the total acidity of the catalysts, except the ZY45 zeolite that exhibited the highest yield of pyridines but the second highest acidity among the samples, as shown in Figure 8a. The total yield of pyridine bases followed the order ZY7 < ZY17 < ZY34 << ZY45, similar to the total acidity of the catalysts, as shown in Figure 8a. The catalytic activity of zeolites depends on several factors, such as the concentration of sites, their acid strength, and accessibility for reactants. The acid strength increases with the Si/Al atomic ratio. The acid strength of zeolites in this study may be assumed more or less constant. Since the BET areas of the zeolites with Si/Al atomic ratios between 7 and 45 are similar, the accessibility of acrolein to acid sites was also similar among the catalysts. As consequence, the total acidity was the most significant property for the conversion.

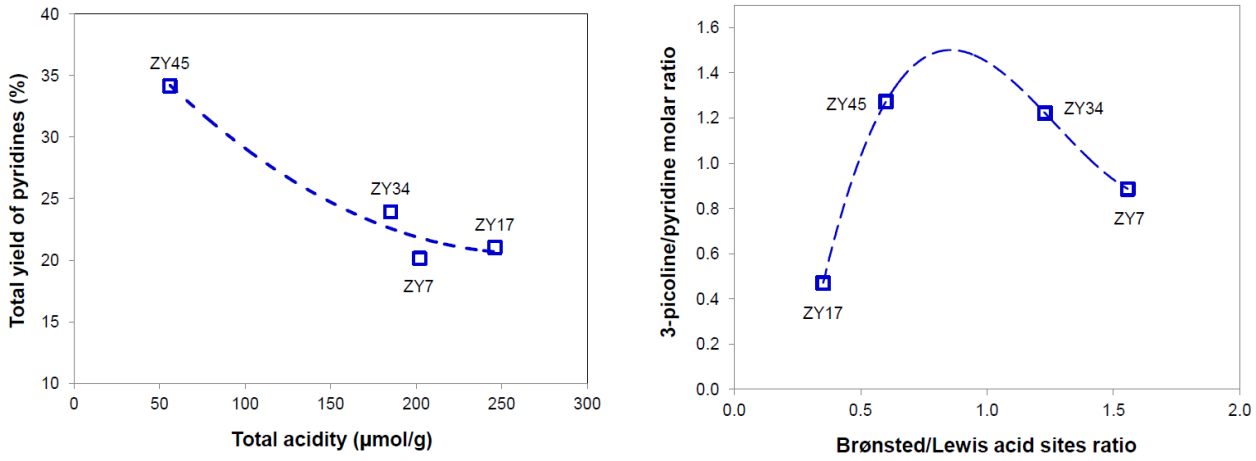


(**a**) (**b**)

**Figure 8.** (**a**) Effect of the catalyst total acidity on the total yield of pyridines and (**b**) effect of the Brønsted/Lewis acid sites ratio on the 3-picoline/pyridine molar ratio.

Furthermore, the type and amount of acid sites influenced the selectivity of pyridine products. As shown in Figure 8b, the Brønsted/Lewis acid sites ratio deviated from unity to lower or higher values, 3-picoline was the main pyridine product. However, the 3-P/Py molar ratio approaches 1 (this is similar amounts of 3-picoline and pyridine) in the BAS/LAS range between 0.6 and 1.3, as with catalysts ZY34 and ZY45. The further increase or decrease of the BAS/LAS ratio originated smaller values of the 3-P/Py molar ratio than unity, and the reaction proceeded preferentially towards pyridine. Remarkably, the formation of pyridine occurred more selectively over LAS than BAS; i.e., the ZY17 zeolite, the catalyst with the smallest BAS/LAS acid sites ratio, exhibited a smaller 3-P/Py molar ratio than the catalyst with the highest BAS/LAS ratio, namely the ZY7 zeolite. Similar results were reported for the reaction between acrolein and ammonia over an HF/MgZSM-5 catalyst, where pyridine was found to be produced over strong LAS, and 3-picoline was formed over BAS and weak LAS [54].

### 2.3. Catalyst Deactivation Behavior

The catalytic activity tests at 360 °C and GHSV = 4994 $h^{-1}$ were monitored with time on stream (TOS). As shown in Figure 9a–c, the activity of the zeolites in the acrolein aminocyclization exhibited differences with TOS. In all cases, the catalysts exhibited a rapid decrease in activity. Both the ZY7 and ZY17 catalysts presented similar behavior, a step decrease in conversion along TOS, reaching 56% and 61% of conversion at 45 min, respectively. Conversely, the decrease of the acrolein conversion for the ZY34 and ZY45 zeolites was less severe during the first 25 min of the process, achieving 65% and 63% of conversion at 45 min, correspondingly. Notably, the catalyst with a Si/Al ratio of 45 showed a steady behavior between 5 and 15 min, with conversions around 92% and 90%. Similarly, a rapid deactivation of ZSM-5 catalysts, due to coke deposited on the catalyst surface, has been reported for the synthesis of pyridines from aldehydes and ammonia [9,10,51,53,55].

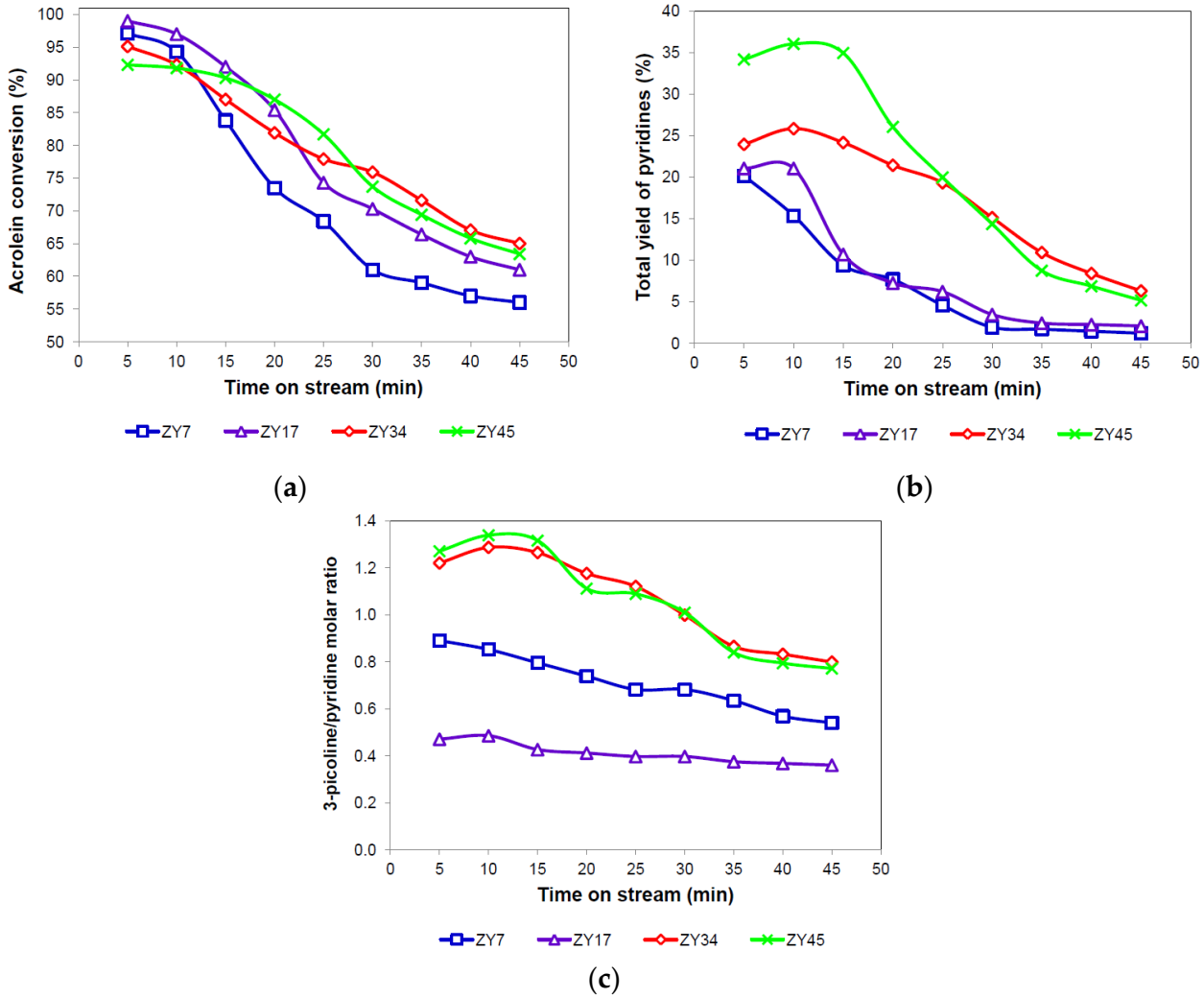


**Figure 9.** (**a**) Acrolein conversion, (**b**) total yield of pyridines, and (**c**) 3-picoline/pyridine molar ratio over the Y-type zeolites with time on stream.

The deactivation of solid acid catalysts during catalytic reactions of organic reactants is commonly caused by the deposition of heavy secondary products, covering the acid sites and blocking the catalyst pores. These carbonaceous compounds, also known as coke, are produced by polymerization reactions of reactants and products [56,57].

The total yield of pyridines with TOS was also influenced by the catalyst, as presented in Figure 9b. Both the ZY7 and ZY17 zeolites showed a gradual decline in the formation of pyridines with values below 10% after 15 min of TOS and approaching 3% as the

minimum value at 45 min. Conversely, the total yield of pyridine bases over the ZY34 catalyst presented a steady behavior between 5 and 20 min, with values around 11%, and smoothly decreased to 7% at 45 min. When using the ZY45 zeolite, pyridines formation maintained higher values than the rest of the catalysts during 25 min, but a significant decrease occurred after 15 min of TOS up to 6% of the total yield of pyridines at 45 min.

Regarding the behavior of pyridine products with TOS, as shown in Figure 9c, the catalysts exhibit a decrease in the 3-P/Py molar ratio in all cases. In the case of the ZY7 and ZY17 catalysts, the change in the pyridine products ratio with TOS was minimal, producing higher amounts of pyridine than 3-picoline throughout the test (3-P/Py < 1). On the other hand, the ZY34 and ZY45 showed a slight increase in the 3-P/Py molar ratio during the first 15 min and a gradual decrease for the rest of the test. Both catalysts maintained higher amounts of 3-picoline than pyridine (3-P/Py > 1) for the initial 30 min. This behavior is consistent with those observed during the reaction with acrolein [10], and formaldehyde with acetaldehyde [50,58] using ZSM-5 zeolites.

The data of the acrolein conversion with TOS were used to establish an equation to model the deactivation of the catalysts during the reaction between acrolein and ammonia. Since the deactivation curves of the Y-type zeolites showed a residual or steady-state activity after initial deactivation the generalized power-law equation (GPLE) deactivation model was considered [59]. The first- and second-order deactivation models are expressed in Equations (1) and (2), respectively:

$$\ln(X - X_s) = \ln(k[W_{cat}/F_{a,0}] - X_s) - k_d t \quad (1)$$

$$\ln\left(\frac{X - X_s}{X + X_s}\right) = \ln\left(\frac{1 - [F_{a,0}X_s/W_{cat}k]}{1 + [F_{a,0}X_s/W_{cat}k]}\right) - [2F_{a,0}X_s k_d/W_{cat}k]t \quad (2)$$

where $X$ is the conversion of acrolein, $X_s$ represents the steady-state conversion, $k$, and $k_d$ are the reaction and deactivation rate constants, in that order; $W_{cat}$ is the weight of catalyst loaded into the reactor; $F_{a,0}$ is the molar flow rate of acrolein; and $t$ is time. The GPLE deactivation models were fitted to the experimental data by non-linear regression, minimizing the sum of square residuals (SSR) as the objective function and discriminated in terms of their determination coefficients ($R^2$).

Figure 10 compares the observed activity of each catalyst and the activity estimated with the GPLE models. It is noticeable that the second-order model showed a slightly better fitting than the first-order.

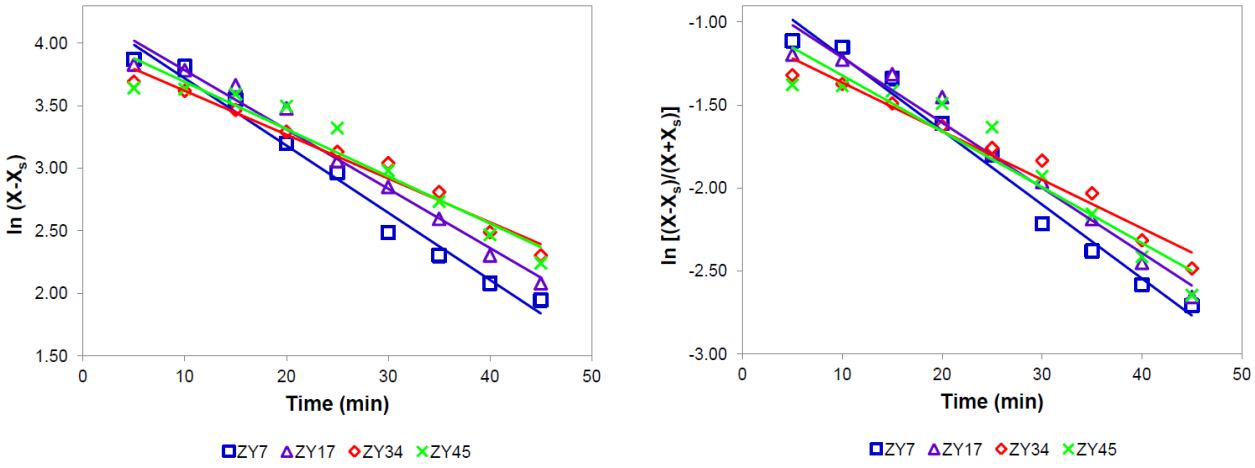


(**a**) (**b**)

**Figure 10.** Fitting of the observed and estimated activity data by the generalized power-law equation (GPLE) models: (**a**) first-order model and (**b**) second-order model.

The minimization results presented in Table 2 showed that both models provide reliable results for all the catalysts. However, the second-order model provided a better fit (lower SSR and higher $R^2$ values) than the first-order model, in agreement with the literature [59–61].

**Table 2.** Reaction and deactivation rate constants and discrimination parameters for the reaction between acrolein and ammonia over the Y-type zeolites.

| Catalyst | $n = 1$ | | | | $n = 2$ | | | |
|---|---|---|---|---|---|---|---|---|
| | $k$ (mol·$g_{cat}^{-1}$·$min^{-1}$) | $k_d$ ($min^{-1}$) | SSR | $R^2$ | $k$ (mol·$g_{cat}^{-1}$·$min^{-1}$) | $k_d$ ($min^{-1}$) | SSR | $R^2$ |
| ZY7 | $2.94 \times 10^{-1}$ | $5.37 \times 10^{-2}$ | 0.08 | 0.98 | 3.02 | $6.11 \times 10^{-2}$ | 0.06 | 1 |
| ZY17 | $3.04 \times 10^{-1}$ | $4.73 \times 10^{-2}$ | 0.08 | 0.98 | 2.98 | $5.04 \times 10^{-2}$ | 0.07 | 1 |
| ZY34 | $2.66 \times 10^{-1}$ | $3.50 \times 10^{-2}$ | 0.05 | 0.98 | 3.62 | $2.98 \times 10^{-2}$ | 0.05 | 1 |
| ZY45 | $2.77 \times 10^{-1}$ | $3.77 \times 10^{-2}$ | 0.17 | 0.93 | 3.37 | $3.68 \times 10^{-2}$ | 0.16 | 0.99 |

For the first-order model, the reaction rate constants slightly increased with the change of the Si/Al atomic ratio from 7 to 17 and decreased for the ZY34 and ZY45 samples. Conversely, the second-order model gave smaller values of the reaction rate constant for the ZY7 and ZY17 catalysts than those of the zeolites with atomic ratios Si/Al = 34 and 45. Furthermore, for both models, the deactivation rate constants of the ZY34 and ZY45 zeolites displayed the smallest values among the samples, in agreement with the rapid decrease of the acrolein conversion with TOS (Figure 9a).

At this point, it is important to mention that there is a lack of information in the literature on the reaction and deactivation kinetic parameters of the synthesis of pyridines. For this type of reaction, it has only been reported the reaction kinetics and the deactivation rate constant for an H-ZSM-5 catalyst in the synthesis of pyridine bases from acetaldehyde, formaldehyde, and ammonia ($k_d$ = 3.61 × $10^{-4}$ $min^{-1}$ at 350 ° C, space-time between 147–440 g/h/mol, molar ratio $NH_3$/aldehyde = 4, and water diluted feed) [62].

### *2.4. Characterization of Spent Catalysts*

Designated as SZY7, SZY17, SZY34, and SZY45, the spent catalysts were characterized to analyze the changes that occurred in the solid samples after the stability test at 360 °C and GHSV = 4994 $h^{-1}$.

Presented in Figure 11, the X-ray diffractograms of the spent catalysts revealed that after the reaction between acrolein and ammonia, the zeolites maintained their crystalline structure. When comparing with the fresh samples, a loss of crystallinity was evidenced by the decrease of the intensity and a shift towards lower values of 2 thetas of the XRD patterns of spent catalysts, presumably caused by the deposition of carbonaceous compounds in agreement with the literature [63]. The average change in the position (2-theta scale) of representative planes of the spent catalysts regarding the fresh zeolites is indicated in Figure 11. In addition, the reflection plane (331) became the most intense reflection in all cases.

As reported in Table 3 and compared with the (311) plane of the fresh solids, the zeolite samples showed an increase in their average crystallite sizes after the reaction, suggesting the deposition of bulky compounds inside the microporous cages, causing the expansion of the unit cell.

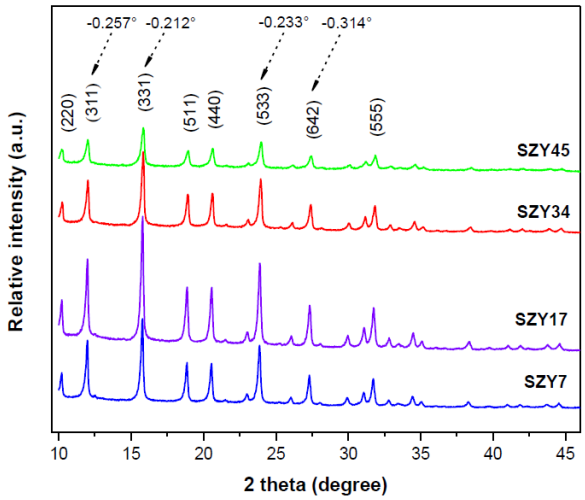


**Figure 11.** X-ray powder diffractograms of the spent Y-type zeolites.

**Table 3.** Physicochemical properties and composition of the spent zeolites.

| Catalyst | $L_{(331)}$ [a] (nm) | Coke Content [b] (wt %) | Element (atom %) [c] | | C/N |
|---|---|---|---|---|---|
| | | | C | N | |
| SZY7 | 38.5 | 25.7 | 35.77 | 5.05 | 7.08 |
| SZY17 | 37.7 | 27.1 | 48.77 | 4.69 | 10.39 |
| SZY34 | 35.2 | 23.1 | 38.99 | 3.97 | 9.82 |
| SZY45 | 27.1 | 22.5 | 31.99 | 4.67 | 6.85 |

[a] Average crystal size, [b] determined by TGA, [c] determined by EDXS.

The Raman spectra of the spent catalysts are shown in Figure 12. The samples exhibited a noticeable shift at 1611 $cm^{-1}$ and a very weak band at 1372 $cm^{-1}$. These bands can be related to coke deposited on the catalyst, attributed explicitly to C=C, and to ring stretches of large polyaromatic compounds, presumably with two-dimensional and sheet-like topology [64–66]. This result suggests that coke deposited on the Y-type zeolites could be produced by secondary reactions of acrolein and olefin intermediates, namely condensation and polymerization, in agreement with previous reports [67,68]. Similarly, in the case of the synthesis of pyridine bases from the reaction between ammonia and aldehydes, it has been determined by solid-state $^{13}C$ NMR and FTIR that the coke formed on ZSM-5 catalysts was constituted by compounds with aliphatic and alkoxyl groups, as well as highly unsaturated polyalkenes and condensed aromatics [69,70].

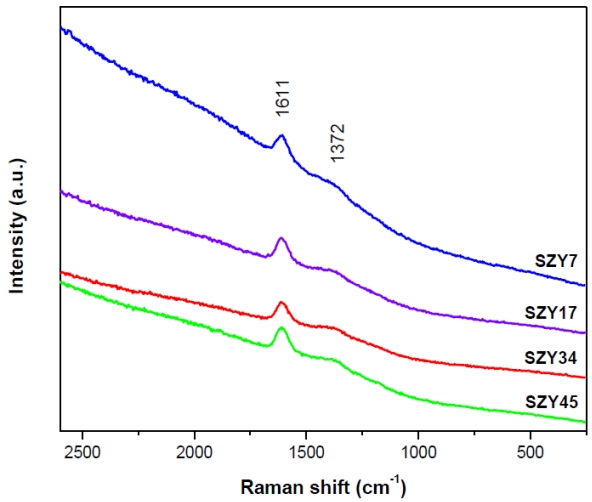


**Figure 12.** Raman spectra of the spent Y-type zeolites.

Shown in Figure 13a, the thermogravimetric analysis of the spent zeolites exhibited two weight losses: the first one between room temperature and 250 °C attributed to the removal of water adsorbed from the reaction, and a second loss between 300–700 °C ascribed to the combustion of the carbonaceous compounds deposited on the catalyst, which varied from 20% to 27% as presented in Table 3.

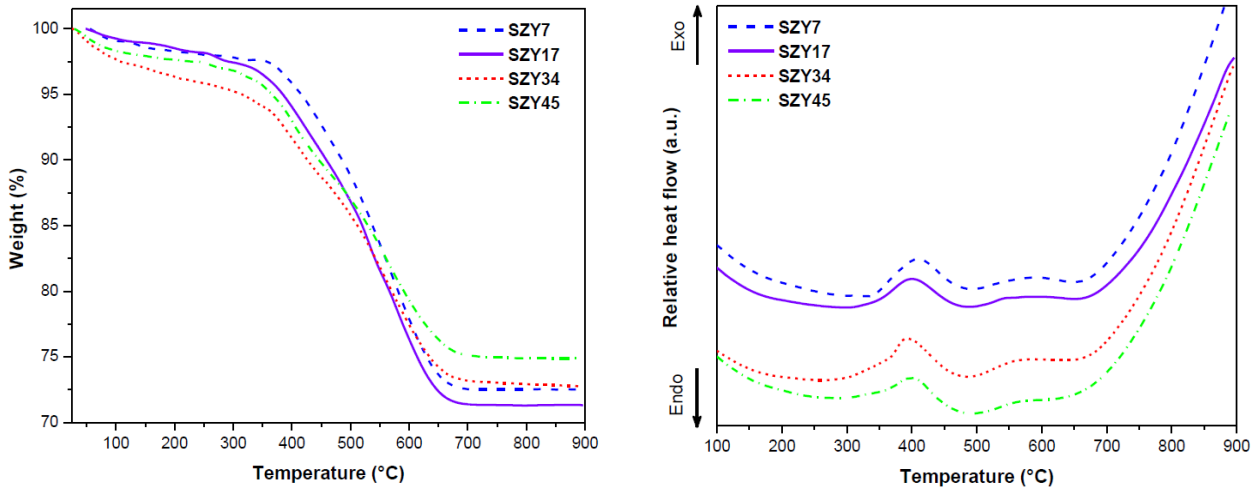


(**a**) (**b**)

**Figure 13.** (**a**) Thermogravimetric analysis and (**b**) differential thermal analysis of the spent Y-type zeolites.

The differential thermal analysis (DTA) presented in Figure 13b evidenced that two exothermic events occurred between 315–660 °C, confirming the combustion of coke deposits from the catalyst and suggesting the presence of different carbonaceous species in agreement with the Raman spectroscopy analysis.

From the estimation of the weight loss between 300–700 °C (Table 3), it is noticeable that the coke content increased with the increment of the Si/Al molar ratio from 7 to 17 and subsequently decreased for the samples with Si/Al molar ratios of 34 and 45. As shown in Figure 14, the amount of coke was corresponding to the pore volume of the fresh ZY7, and ZY17 catalysts, while the decrease of the coke content in the spent ZY34 and ZY45 samples can be explained by their larger pore volume and surface areas.

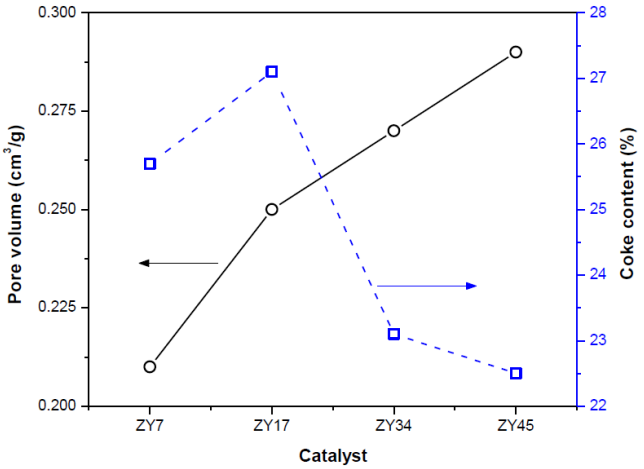


**Figure 14.** Comparison of the pore volume of the fresh zeolites and the coke content of spent catalysts.

The SEM micrographs of the spent catalysts, presented in Figure 15, showed zeolite grains with the same morphology as the fresh samples. Furthermore, it was revealed that

the porosity of the zeolites was preserved. The similarity in micromorphology and surface texture between the fresh and spent catalysts suggested that the carbonaceous compounds could be deposited uniformly inside the porous system and on the outer surface of the zeolites. On the other hand, it was observed an increase in the average grain size of the catalysts after the reaction. The average increment was from 400 nm to 600 nm in the ZY17 and ZY34 catalysts, as shown in the insertions of Figure 15. In the SZY7 and SZY45 samples, an increase was observed in 200 nm and 800 nm particles, respectively.

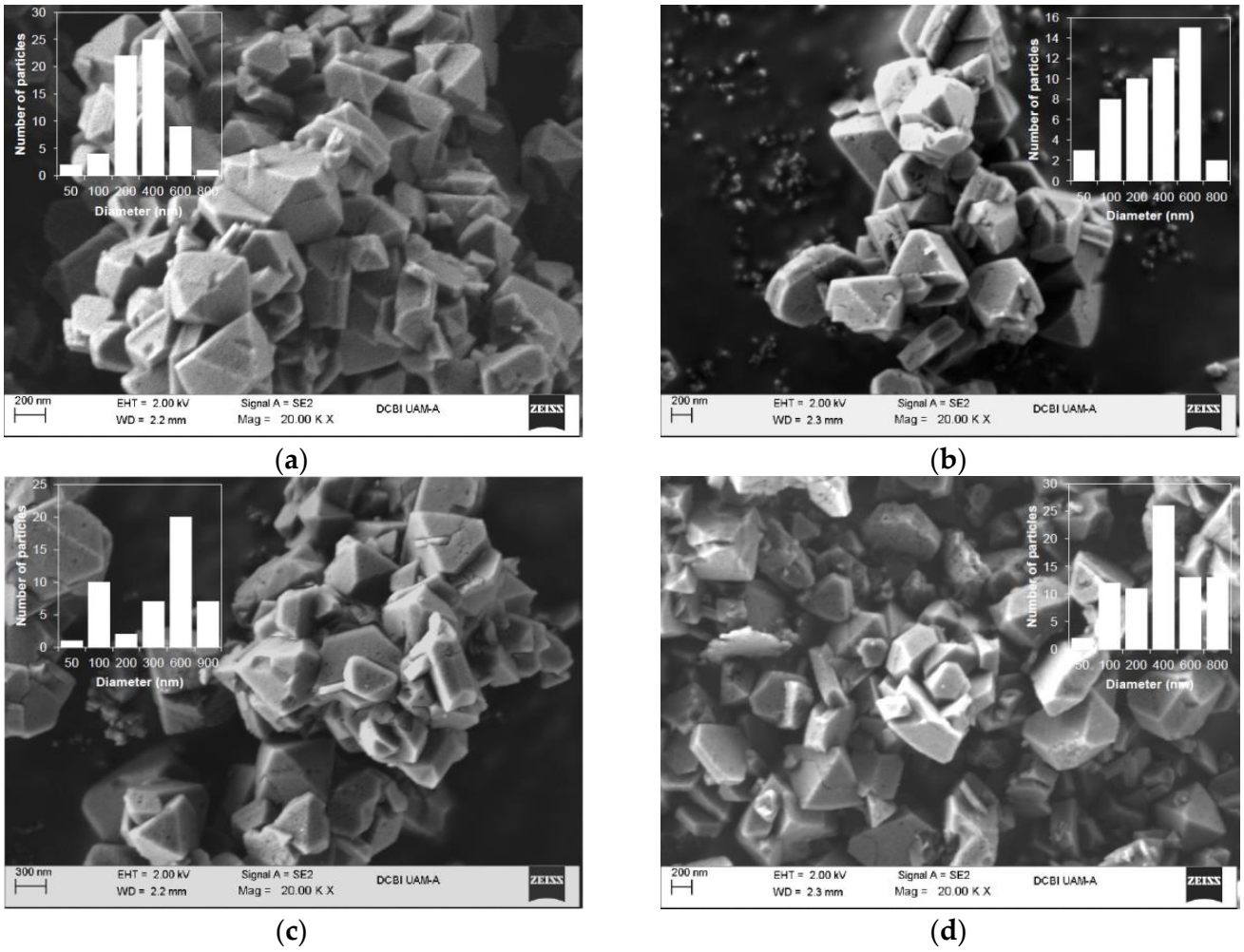


**Figure 15.** Scanning electron micrographs and particle size distributions of the spent zeolites: (**a**) SZY7, (**b**) SZY17, (**c**) SZY34, and (**d**) SZY45.

The elemental analysis by EDXS confirmed that a large quantity of carbon was deposited on the surface of the zeolite, as reported in Table 3. Additionally, nitrogen was also identified, in proportions between 4 and 5 atom % resulting in C/N atomic ratios between 6.8 and 10.4, in agreement with a previous report [55]. From these compositions, it can be inferred that in addition to heavy compounds derived from aldehydes, the pyridine products and intermediates can also be strongly adsorbed on the acid sites of the catalysts, preventing the reactants from interacting, and being part of the carbonaceous compounds deposited within the porous system, decreasing the activity of the catalyst.

From the above results, it is proposed that the reaction between acrolein and ammonia over Y-type zeolites occurred according to the reaction scheme depicted in Figure 16. Under the reaction conditions of this study (low reaction temperature and $NH_3$/acrolein molar ratio = 2), acrolein was partially converted to cracking products, namely acetaldehyde, and formaldehyde. These aldehydes could not produce pyridine bases since there was not enough $NH_3$ to make them react and were easily removed from the reactor due to the high

gas hourly space velocity (GHSV = 4994 $h^{-1}$). On the other hand, acrolein and ammonia react over acid sites to produce propylene imine, as previously reported [54]. Then, this intermediate can undergo a Michael addition reaction with another propylene imine over Brønsted or weak Lewis acid sites, closing the ring structure and producing 3-picoline with the liberation of ammonia. Alternatively, propylene imine can condensate and cyclize with another propylene imine by a Diels-Alder reaction over Lewis acid sites, producing pyridine [71,72]. Due to its basic nature and as suggested by the EDXS results of the spent catalysts, 3-picoline, and pyridine can be strongly absorbed over acid sites, being part of the coke deposited in the catalyst.

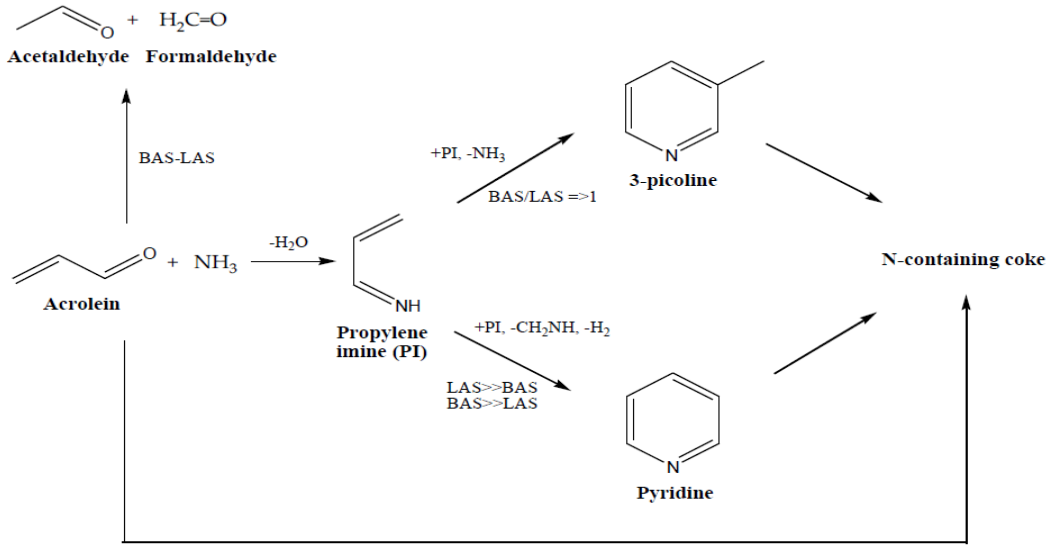


**Figure 16.** Reaction routes for acrolein and ammonia over the Y-type zeolites.

## 3. Materials and Methods

### *3.1. Materials*

Y-type zeolites with Si/Al atomic ratios of 7, 17, 34, and 45 were acquired from Zeolyst International (Conshohocken, PA, USA). Previous to the characterization and the catalytic activity experiments, the samples were calcined at 450 °C in an electrical furnace for 4 h, cooled down to room temperature, and passed through 100 mesh. Finally, the samples were identified as ZY7, ZY17, ZY34, and ZY45, where the number indicates the Si/Al atomic ratio. Acrolein was obtained from Sigma-Aldrich (Toluca, México) and used with any further purification.

### *3.2. Characterization of Catalysts*

The structural features of the Y-type zeolites were confirmed by X-ray diffraction, UV-vis, and Raman spectroscopies. A Bruker AXS model D8 diffractometer was used for the XRD analysis, with CuKα radiation (1.5406 Å). The crystalline structure of the zeolites was verified by comparison of the obtained diffractograms with the crystallographic cards of the Joint Committee on Power Diffraction Standards (JCPDS). The average crystal sizes were estimated from the most intense reflection according to the Scherrer equation: $L = 0.9 \cdot \lambda / \beta \cdot \cos\theta$, where L is the crystal size, λ is the X-ray wavelength, β is the line broadening, and θ is the Bragg angle [73].

The UV-vis spectroscopy analysis of the solids was carried out with a spectrophotometer Varian Cary 100 (Agilent Technologies, Mexico city, Mexico) at 25 °C. The powder samples sieved through 100 mesh were analyzed between 200 and 800 nm with a 1 nm sensibility.

The Raman spectra of the zeolites were obtained with a spectrometer Renishaw inVia (Renishaw Mexico, Apodaca, México) equipped with a cooled CCD detector and a

holographic super-Notch filter to remove the elastic scattering, using the green line laser λ = 532 nm, power 9 mW, 1 mW on the sample. The spectral resolution was ca. 3 $cm^{-1}$ and the spectra acquisition consisted of 5 accumulations of 10 s.

The zeolite samples were studied by thermogravimetric analysis in a thermal analyzer model SDT Q600 from TA Instruments, in a temperature range between 25 °C and 900 °C with a heating rate of 10 °C·$min^{-1}$ and an airflow of 10 mL·$min^{-1}$.

The surface acidity of the Y-type zeolites was studied by Fourier transform infrared spectroscopy with adsorbed pyridine (IR-Py) in Nicolet equipment, model 170-SX (Thermo Fisher Scientific Inc., Mexico city, Mexico). In a typical procedure, the powder sample was pressed forming a thin disk, and placed into a glass cell where temperature and vacuum were controlled. Prior to pyridine adsorption, the sample was pretreated with a vacuum at $1 \times 10^{-3}$ Torr with subsequent heating at 300 °C at a rate of 20 °C·$min^{-1}$, and cooling to room temperature. Then, a mixture of nitrogen and pyridine (4%) was fed to the cell to be in contact with the catalyst sample for 15 min at 25 °C for the chemisorption process.

Physisorbed pyridine was desorbed from the sample by vacuum, and the FTIR spectra were obtained in situ at 350 °C. The Brønsted acid sites were identified by their interaction with pyridine, which exhibits bands at 1540 $cm^{-1}$ and 1640 $cm^{-1}$, while the coordination of pyridine with Lewis acid sites results in the appearance of typical bands at 1447–1460 $cm^{-1}$, 1580 $cm^{-1}$ and 1600 $cm^{-1}$ [39]. The amount of Brønsted and Lewis acid sites was determined considering the integrated areas of the bands at 1540 $cm^{-1}$ and 1450 $cm^{-1}$, correspondingly, and the integrated molar extinction coefficients reported by Emeis [74] of $\varepsilon_B$ = 1.67 cm/μmol for Brønsted acid sites and $\varepsilon_L$ = 2.22 cm/μmol for Lewis acid sites according to the Beer's law.

For the Al quantification, each sample was subjected to acid digestion with aqua regia ($HNO_3$ + 3 HCl) at 50 °C for 20 h. Subsequently, the filtered liquid extract was analyzed in a Perkin Elmer Atomic absorption spectrometer model AAnalyst 400 with a calibration curve prepared with the commercial Al standard of the same company.

The $N_2$ physisorption of the solids was determined at −196 °C using Micromeritics ASAP-2450 equipment. In a typical analysis, the sample was pretreated at 300 °C under vacuum at $1 \times 10^{-3}$ Torr for 3 h. The adsorption isotherm of each solid was determined by the successive charges of $N_2$ introduced into the sample container, increasing the pressure and allowing 15 s to pass between each charge to achieve balance. The specific surface area, the pore volume, and the pore size of each sample were estimated considering the Brunauer, Emmet, and Teller model (BET) [75], the t-plot method, and the Barret, Joynet, and Halenda model (BJH) [76], respectively.

Observations of the Y-type zeolites were accomplished in a scanning electron microscope (SEM) Zeiss Supra 55 VP coupled with a probe with energy-dispersive X-ray spectroscopy (EDXS) to obtain the respective spectra, as well as qualitative and quantitative elemental analyses of the samples. For their observation, the fresh and spent catalyst powders were spread on graphite and copper tapes, respectively.

### *3.3. Catalytic Activity Tests*

The gas-phase reactions between acrolein and ammonia were performed at 1 atm and controlled temperature in a system comprised of an acrolein saturator vessel, a stainless steel fixed-bed reactor (32 cm length and 1 cm internal diameter), and an electrical furnace provided with a thermocouple and an electronic temperature controller.

Initially, 0.30 g of catalyst ($W_{cat}$) was loaded into the reactor over a porous fiberglass bed and activated by heating at 450 °C for 30 min with an $N_2$ flow at 50 mL·$min^{-1}$. Afterward, the reactor was set to the reaction temperature (360 °C), maintaining the gas flow, and stabilized for 30 min. Subsequently, the acrolein vapor contained in the saturator vessel at 21 °C was carried out with a 50 mL·$min^{-1}$ $N_2$ flow and fed to the reactor. Due to the feeding conditions of this mixture, the gas hourly space velocity (GHSV) was 4994 $h^{-1}$. Simultaneously, gaseous ammonia ($NH_3$) was directly fed at the reactor inlet from a container tank to achieve an $NH_3$/acrolein molar ratio equal to 2. To mainly exhibit the

influence of the catalyst properties on the reaction, no water was added to the feed stream, and the values of reaction temperature and $NH_3$/acrolein molar ratio were chosen to diminish their positive effect on the formation of pyridine bases.

The output flow from the reactor passed through a gas sampling point, cooled in a condenser at 6 °C, and collected in an ice-cold trap. The acrolein at the input and output of the reactor, and the reaction products, were analyzed in a gas chromatograph GOWMAC 750 equipped with a packed column 15% FFAP Chrom W-A/W 80/100 (2 m × 1/8 inch) and a flame ionization detector. The acrolein conversion ($X$) and the product yield ($Y_i$) were calculated according to Equations (1) and (2), respectively:

$$X(\%) = \frac{N_{a,in} - N_{a,out}}{N_{a,in}} \cdot 100 \tag{3}$$

$$Y_i(\%) = \frac{C_i}{C_{a,in}} \cdot 100 \tag{4}$$

where $N_{a,in}$ and $N_{a,out}$ are the moles of acrolein at the inlet and outlet stream of the reactor, correspondingly; $C_i$ and $C_{a,in}$ are the carbon moles in the product $i$ and fed acrolein, respectively.

### *3.4. Catalyst Deactivation Behavior*

The catalytic activity tests at 360 °C and GHSV = 4994 $h^{-1}$ were monitored with time on stream (TOS) until the total yield of pyridine compounds was below 10%. The acrolein conversion data with TOS was used to model the deactivation behavior of each catalyst during the aminocyclization reaction considering the deactivation kinetic model proposed by Fuentes [59],

$$-\frac{da}{dt} = k_d(a^n - a_s^n) \tag{5}$$

where $a$ is the activity, $k_d$ is the deactivation rate constant, $a_s$ is the steady-state activity, and $n$ is the deactivation order.

The kinetic deactivation equations and the experimental results were fitted by non-linear regression, minimizing the sum of square residuals ($SSR$) as the objective function by use of the Microsoft Excel Solver tool, and discriminated in terms of the determination coefficient ($R^2$), according to the following equations:

$$SSR = \sum (y_{i,est} - y_{i,obs})^2 \tag{6}$$

$$R^2 = 1 - \frac{SSR}{TSS} \tag{7}$$

$$TSS = \sum (y_{i,obs} - \overline{y}_{obs})^2 \tag{8}$$

where $y_{i,est}$ and $y_{i,obs}$ are the estimated and observed values of the dependent variable, respectively, $TSS$ is the total sum of squares, and $\overline{y}_{obs}$ is the mean of the observed values of the dependent variable.

### *3.5. Characterization of Deactivated Catalysts*

After the deactivation tests, the spent zeolites, denoted as SZY7, SZY17, SZY34, and SZY45, were characterized by XRD, Raman spectroscopy, TGA, and SEM-EDXS under the same conditions as mentioned in Section 3.2.

## 4. Conclusions

The Y-type zeolites with Si/Al atomic ratios between 7 and 45 were active as catalysts in the reaction between acrolein and ammonia. The acrolein conversion improved with the

increase of the total acidity per gram of the catalyst, reaching higher conversion using the zeolite with Si/Al = 17.

The production of pyridine bases was inversely proportional to the total acidity of the catalysts which exhibited similar textural properties (large surface areas, pore volume as well as micro- and mesoporosity) achieving the maximum yield of pyridines (3-picoline + pyridine) using the catalyst with Si/Al = 45. The type and amount of acid sites influenced the selectivity of pyridine products. 3-picoline was produced in higher amounts than pyridine (highest value of the 3-picoline/pyridine molar ratio) when the catalyst presented Brønsted/Lewis acid sites ratios approaching one (in the range of 0.6 and 1.3). The reaction proceeded preferentially towards pyridine with the further decline or increase of the Brønsted/Lewis acid sites ratio. Additionally, the formation of pyridine occurred more selectively over LAS than BAS.

The stability of the catalysts with time on stream was influenced by their textural properties, as indicated by the deactivation tests and the proposed kinetic deactivation models. The loss of activity was caused by the uniform deposition of large amounts of coke on the catalyst surface and within the inner porous network of the zeolites according to the characterization of the spent zeolites by DRX, TGA, and SEM. Additionally, the Raman spectroscopy analysis of the spent catalysts indicated that coke could be composed of large polyaromatic compounds. EDXS results showed that pyridine products and their intermediates can also be part of the coke deposited.

**Author Contributions:** Conceptualization, I.P.-R., J.L.C. and J.S.; methodology, I.P.-R., J.L.C. and J.S.; software, I.P.-R.; validation, J.L.C. and J.S.; formal analysis, I.P.-R., J.L.C., J.S., R.L.-M., D.A.-B., B.Z., J.N.-B. and N.N.G.-H.; investigation, I.P.-R. and J.L.C.; resources, J.L.C., J.S., R.L.-M., D.A.-B., B.Z., J.N.-B.; data curation, I.P.-R. and J.L.C.; writing—original draft preparation, I.P.-R.; writing—review and editing, I.P.-R., J.L.C., J.S., R.L.-M., D.A.-B., B.Z., J.N.-B. and N.N.G.-H.; visualization, I.P.-R.; supervision, J.L.C. and J.S.; project administration, J.L.C.; funding acquisition, J.L.C. and J.S. All authors have read and agreed to the published version of the manuscript.

**Funding:** This research received no external funding.

**Data Availability Statement:** Not applicable.

**Acknowledgments:** The authors thank the Instituto Politécnico Nacional, the Universidad Autónoma Metropolitana-Azcapotzalco, and the Instituto Mexicano del Petróleo for the support to develop this research. The Scanning Electron Microscopy Laboratory of the Division of Basic Sciences and Engineering of the Universidad Autónoma Metropolitana-Azcapotzalco is acknowledged for the characterization of the catalyst samples by SEM-EDXS. I.P.R. and J.L.C. appreciate the support of the company Síntesis y Aplicaciones Industriales, S.A.

**Conflicts of Interest:** The authors declare no conflict of interest.

## References

1. Weissermel, K.; Arpe, H.J. Chapter 7: Oxydation products of ethylene. In *Industrial Organic Chemistry*, 3rd ed.; VCH Publishers, Inc.: Weinheim, Germany, 1997; pp. 143–190.
2. Shimizu, S.; Abe, N.; Iguchi, A.; Sato, H. Synthesis of pyridine bases: General methods and recent advances in gas phase synthesis over ZSM-5 zeolite. *Catal. Surv. Jpn.* **1998**, *2*, 71–76. [CrossRef]
3. Shimizu, S.; Watanabe, N.; Kataoka, T.; Shoji, T.; Abe, N.; Morishita, S.; Ichimura, H. Pyridine and pyridine derivatives. In *Ullmann's Encyclopedia of Industrial Chemistry*; Wiley-VCH Verlag GmbH & Co. KGaA: Weinheim, Germany, 2012; pp. 557–589.
4. Scriven, E.F.V.; Murugan, R. Pyridine and pyridine derivatives. In *Kirk-Othmer Encyclopedia of Chemical Technology*; John Wiley & Sons, Inc.: Hoboken, NJ, USA, 2005; pp. 1–53.
5. Sagitullin, R.S.; Shkil', G.P.; Nosonova, I.I.; Ferber, A.A. Synthesis of pyridine bases by the Chichibabin method (review). *Chem. Heterocycl. Comp.* **1996**, *32*, 127–140. [CrossRef]
6. Reddy, K.S.K.; Srinivasakannan, C.; Raghavan, K.V. Catalytic vapor phase pyridine synthesis: A process review. *Catal. Surv. Asia* **2012**, *16*, 28–35. [CrossRef]
7. Tschitschibabin, A.E. Über kondensationen der aldehyde mit ammonik zu pyridinbasen. *J. Für Prakt. Chem.* **1924**, *107*, 122–128. [CrossRef]

8. Sato, H.; Shimizu, S.; Abe, N.; Hirose, K. Vapor phase synthesis of pyridine bases from aldehydes and ammonia over pentasil zeolites. Zeolites and related microporous materials: State of the art 1994. In *Studies in Surface Science and Catalysis*; Hölderich, W., Karge, H.G., Weitkamp, J., Pfeifer, H., Eds.; Elsevier Science B.V.: Amsterdam, The Netherlands, 1994; Volume 84, pp. 1951–1958.
9. Reddy, K.S.K.; Sreedhar, I.; Raghavan, K.V. Interrelationship of process parameters in vapor phase pyridine synthesis. *App. Catal. A Gen.* **2008**, *339*, 15–20. [CrossRef]
10. Zhang, X.; Wu, Z.; Liu, W.; Chao, Z.S. Preparation of pyridine and 3-picoline from acrolein and ammonia with HF/MgZSM-5 catalyst. *Catal. Commun.* **2016**, *80*, 10–14. [CrossRef]
11. Luo, C.W.; Chao, Z.S. Unsaturated aldehydes: A novel route for the synthesis of pyridine and 3-picoline. *RSC Adv.* **2015**, *5*, 54090–54101. [CrossRef]
12. Luo, C.W.; Li, A. Synthesis of 3-picoline from acrolein dimethyl acetal and ammonia over $NH_4$F-HF treated ZSM-5. *React. Kinet. Mech. Catal.* **2018**, *125*, 365–380. [CrossRef]
13. Liu, L.; Ye, X.P.; Bozell, J.J. A comparative review of petroleum-based and bio-based acrolein production. *ChemSusChem* **2012**, *5*, 1162–1180. [CrossRef]
14. Galadima, A.; Muraza, O. A review on glycerol valorization to acrolein over solid acid catalysts. *J. Taiwan Inst. Chem. Eng.* **2016**, *67*, 29–44. [CrossRef]
15. Pala Rosas, I.; Contreras Larios, J.L.; Zeifert, B.; Salmones Blásquez, J. Catalytic dehydration of glycerine to acrolein. In *Glycerine Production and Transformation—An Innovative Platform for Sustainable Biorefinery and Energy*; Frediani, M., Bartoli, M., Rosi, L., Eds.; IntechOpen: London, UK, 2019; pp. 9–27.
16. Kong, P.S.; Aroua, M.K.; Daud, W.M.A.W. Conversion of crude and pure glycerol into derivatives: A feasibility evaluation. *Renew. Sustain. Energy Rev.* **2016**, *63*, 533–555. [CrossRef]
17. Van Der Gaag, F.J.; Louter, G.; Oudejans, J.C.; Van Bekkum, H. Reaction of ethanol and ammonia to pyridines over zeolite ZSM-5. *Appl. Catal.* **1986**, *26*, 191–201. [CrossRef]
18. Grigor'eva, N.G.; Filippova, N.A.; Tselyutina, M.I.; Kutepov, B.I. Synthesis of pyridine and methylpyridines over zeolite catalysts. *Appl. Petrochem. Res.* **2015**, *5*, 99–104. [CrossRef]
19. Van Donk, S.; Janssen, A.H.; Bitter, J.J.; de Jong, K.P. Generation, characterization, and impact of mesopores in zeolite catalysts. *Catal. Rev.* **2003**, *45*, 297–319. [CrossRef]
20. Perego, C.; Bosetti, A. Biomass to fuels: The role of zeolite and mesoporous materials. *Microporous Mesoporous Mater.* **2011**, *144*, 28–39. [CrossRef]
21. Bu, L.; Nimlos, M.R.; Robichaud, D.J.; Kim, S. Diffusion of aromatic hydrocarbons in hierarchical mesoporous H-ZSM-5 zeolite. *Catal. Today* **2018**, *312*, 73–81. [CrossRef]
22. Zhang, H.; Samsudin, I.B.; Jaenicke, S.; Chuah, G.K. Zeolites in catalysis: Sustainable synthesis and its impact on properties and applications. *Catal. Sci. Technol.* **2022**, *12*, 6024. [CrossRef]
23. Subba Rao, Y.V.; Kulkarni, S.J.; Subrahmanyam, M.; Rama Rao, A.V. A novel acylative cyclization reaction of phenol over modified Y zeolites. *J. Chem. Soc. Chem. Commun.* **1993**, *3212*, 1456–1457.
24. Vajglová, Z.; Kumar, N.; Mäki-Arvela, P.; Eranen, K.; Peurla, M.; Hupa, L.; Nurmi, M.; Toivakka, M.; Murzin, D.Y. Synthesis and physicochemical characterization of shaped catalysts of β and Y zeolites for cyclization of citronellal. *Ind. Eng. Chem. Res.* **2019**, *58*, 18084–18096. [CrossRef]
25. Yu, W.; Bian, F.; Gao, Y.; Yang, L.; Liu, Z.L. Y-zeolite-catalyzed cyclizations of terpenols. *Adv. Synth. Catal.* **2006**, *348*, 59–62. [CrossRef]
26. Pérez-Mayoral, E.; Matos, I.; Fonseca, I.; Cejka, J. Zeolites efficiently promote the cyclization of nonactivated unsaturated alcohols. *Chem. Eur. J.* **2010**, *16*, 12079–12082. [CrossRef]
27. Kim, H.J.; Seo, G.; Kim, J.N.; Choi, K.H. HY zeolite catalyzed one-pot synhtesis of 2,3-dihydro-2,2-dimethylbenzofurans from aryl methallyl ethers. *Bull. Korean Chem. Soc.* **2004**, *25*, 1726–1728.
28. Shimizu, S.; Abe, N.; Iguchi, A.; Dohba, M.; Sato, H.; Hirose, K. Synthesis of pyridine bases on zeolite catalysts. *Microporous Mesoporous Mater.* **1998**, *21*, 447–451. [CrossRef]
29. Treacy, M.M.J.; Higgins, J.B. *Collection of Simulated XRD Patterns for Zeolites*; Elsevier B.V.: Amsterdam, The Netherlands, 2001; pp. 146–153.
30. Lutz, W.; Rüscher, C.H.; Gesing, T.M. Investigations of the mechanism of dealumination of zeolite Y by steam: Tuned mesopore formation versus the Si/Al ratio. *Stud. Surf. Sci. Catal.* **2004**, *154*, 1411–1417.
31. Li, C.; Wu, Z. Chapter 11 Microporous materials characterized by vibrational spectroscopies. In *Handbook of Zeolite Science and Technology*; Auerbach, S.M., Carrado, K.A., Dutta, P.K., Eds.; CRC Press: Boca Raton, FL, USA, 2003; pp. 423–514.
32. Meng, Y.; Genuino, H.C.; Kuo, C.H.; Huang, H.; Chen, S.Y.; Zhang, L.; Rossi, A.; Suib, S.L. One-step hydrothermal synthesis of Manganese-Containing MFI-type zeolite, Mn-ZSM-5, characterization, and catalytic oxydation of hydrocarbons. *J. Am. Chem. Soc.* **2013**, *135*, 8594–8605. [CrossRef]
33. Dutta, P.K.; Twu, J. Influence of framework Si/Al ratio on the Raman spectra of faujasitic zeolites. *J. Phys. Chem.* **1991**, *95*, 2498–2501. [CrossRef]
34. Dutta, P.K.; Rao, K.M.; Park, J.Y. Correlation of Raman spectra of zeolites with framework architecture. *J. Phys. Chem.* **1991**, *95*, 6654–6656. [CrossRef]

35. Brémard, C.; Le Maire, M. Low-frequency Raman spectra of dehydrated faujasitic zeolites. *J. Phys. Chem.* **1993**, *97*, 9695–9702. [CrossRef]
36. Yu, Y.; Xiong, G.; Li, C.; Xiao, F.S. Characterization of aluminosilicate zeolites by UV Raman spectroscopy. *Microporous Mesoporous Mater.* **2001**, *46*, 23–34. [CrossRef]
37. Laughlin, R.B.; Joannopoulous, J.D. Phonons in amorphous silica. *Phys. Rev. B* **1977**, *16*, 2942–2952. [CrossRef]
38. De Man, A.J.M.; van Beest, B.H.W.; Leslie, M.; van Santen, R.A. Lattice dynamics of zeolitic silica polymorphs. *J. Phys. Chem.* **1990**, *94*, 2524–2534. [CrossRef]
39. Parry, E.P. An infrared study of pyridine adsorbed on acidic solids. Characterization of surface acidity. *J. Catal.* **1963**, *2*, 371–379. [CrossRef]
40. Sandoval-Díaz, L.E.; González-Amaya, J.A.; Trujillo, C.A. General aspects of zeolite acidity characterization. *Microporous Mesoporous Mater.* **2015**, *215*, 229–243. [CrossRef]
41. de Castro, P.R.D.S.; Barreto Maia, A.A.; Simões Angélica, R. Study of the thermal stability of faujasite zeolite synthesized from kaolin waste from the Amazon. *Mater. Res.* **2019**, *22*, e20190321. [CrossRef]
42. Ayad, Z.; Hussein, H.Q.; Al-Tabbakh, B.A. Synthesis and characterization of high silica HY zeolite by basicity reduction. *AIP Conf. Proc.* **2020**, *2213*, 020168.
43. Leofanti, G.; Padovan, M.; Tozzola, G.; Venturelli, B. Surface area and pore texture of catalysts. *Catal. Today* **1998**, *41*, 207–219. [CrossRef]
44. Thommes, M.; Kaneko, K.; Neimark, A. Physisorption of gases, with special reference to the evaluation of surface area and pore size distribution (IUPAC Technical Report). *Pure Appl. Chem.* **2015**, *87*, 1051–1069. [CrossRef]
45. Huang, Q.; Wang, J.; Sun, Y.; Li, X.; Wang, X.; Zhao, Z. Gas-sensing properties of composites of Y-zeolite and $SnO_2$. *J. Mater. Sci.* **2018**, *53*, 6729–6740. [CrossRef]
46. Liu, M.; Ren, Y.; Wu, J.; Wang, Y.; Chen, J.; Lei, X.; Zhu, X. Effect of cations on the structure, physico-chemical properties and photocatalytic behaviors of silver-doped zeolite Y. *Microporous Mesoporous Mater.* **2020**, *293*, 109800. [CrossRef]
47. Taufiqurrahmi, N.; Mohamed, A.R.; Bhatia, S. Nanocrystalline zeolite Y: Synthesis and sharacterization. *IOP Conf. Ser. Mater. Sci. Eng.* **2011**, *17*, 012030. [CrossRef]
48. Li, A.; Luo, C.; Liu, Y.; Li, L.; Lin, Y.; Liu, K.; Zhou, C. Zn-promoted Hβ zeolite for gas-phase catalyzed aza-heterocyclic-aromatization of acrolein dimethyl acetal and aniline to quinolines. *Mol. Catal.* **2020**, *486*, 110833. [CrossRef]
49. Martinuzzi, I.; Azizi, Y.; Devaux, J.F.; Tretjak, S.; Zahraa, O.; Leclerc, J.P. Reaction mechanism for glycerol dehydration in the gas phase over a solid acid catalyst determined with on-line gas chromatography. *Chem. Eng. Sci.* **2014**, *116*, 118–127. [CrossRef]
50. Kuppi Reddy, S.K.R.; Sreedhar, I.; Raghavan, K.V.; Kulkarni, S.J.; Ramakrishna, M. Optimization of vapor phase pyridine synthesis hindered by rapid catalyst deactivation. *Int. J. Chem. React. Eng.* **2008**, *6*, 1–20. [CrossRef]
51. Liu, Y.; Yang, H.; Jin, F.; Zhang, Y.; Li, Y. Synthesis of pyridine and picolines over Co-modified HZSM-5 catalyst. *Chem. Eng. J.* **2008**, *136*, 282–287. [CrossRef]
52. Luo, C.W.; Li, A.; An, J.F.; Feng, X.Y.; Zhang, X.; Feng, D.D.; Chao, Z.S. The synthesis of pyridine and 3-picoline from gas-phase acrolein diethyl acetal with ammonia over ZnO/HZSM-5. *Chem. Eng. J.* **2015**, *273*, 7–18. [CrossRef]
53. Zhang, W.; Duan, S.; Zhang, Y. Enhanced selectivity in the conversion of acrolein to 3-picoline over bimetallic catalyst 4.6%Cu–1.0%Ru HZSM-5 (38) with hydrogen as carrier gas. *React. Kinet. Mech. Catal.* **2019**, *127*, 391–411. [CrossRef]
54. Zhang, X.; Wu, Z.; Chao, Z.S. Mechanism of pyridine bases prepared from acrolein and ammonia by in situ infrared spectroscopy. *J. Mol. Catal. A Chem.* **2016**, *411*, 19–26. [CrossRef]
55. Kumar Reddy, K.S.; Sreedhar, I.; Venkateshwar, S.; Vijay Raghavan, K. Behavior of a deactivating HZSM-5 with varying $Al^{3+}$ content in vapor phase aminocyclization. *Catal. Lett.* **2008**, *125*, 110–115. [CrossRef]
56. Guisnet, M.; Magnoux, P. Deactivation by coking of zeolite catalysts. Prevention of deactivation. Optimal conditions for regeneration. *Catal. Today* **1997**, *36*, 477–483. [CrossRef]
57. Guisnet, M.; Magnoux, P. Organic chemistry of coke formation. *Appl. Catal. A Gen.* **2001**, *212*, 83–96. [CrossRef]
58. Jin, F.; Cui, Y.; Li, Y. Effect of alkaline and atom-planting treatment on the catalytic performance of ZSM-5 catalyst in pyridine and picolines synthesis. *Appl. Catal. A Gen.* **2008**, *350*, 71–78. [CrossRef]
59. Fuentes, G.A. Catalyst deactivation and steady-state activity: A generalized power-law equation model. *Appl. Catal.* **1985**, *15*, 33–40. [CrossRef]
60. Argyle, M.D.; Frost, T.S.; Bartholomew, C.H. Cobalt Fischer–Tropsch catalyst deactivation modeled using generalized power law expressions. *Top. Catal.* **2014**, *57*, 415–429. [CrossRef]
61. Fadaeerayeni, S.; Shan, J.; Sarnello, E.; Xu, H.; Wang, H.; Cheng, J.; Li, T.; Toghiani, H.; Xiang, Y. Nickel/gallium modified HZSM-5 for ethane aromatization: Influence of metal function on reactivity and stability. *Appl. Catal. A Gen.* **2020**, *601*, 117629. [CrossRef]
62. Kuppi Reddy, S.K.R.; Sreedhar, I.; Raghavan, K.V. Kinetic studies on vapour phase pyridine synthesis and catalyst regeneration studies. *Can. J. Chem. Eng.* **2011**, *89*, 854–863. [CrossRef]
63. Bauer, F.; Karge, H.G. Characterization of coke on zeolites. In *Characterization II*; Molecular Sieves. Science and Technology; Karge, H.G., Weitkamp, J., Eds.; Springer: Berlin/Heidelberg, Germany, 2007; Volume 5, pp. 249–364.
64. Li, C.; Stair, P.C. Utraviolet Raman spectroscopy characterization of coke formation inzeolites. *Catal. Today* **1997**, *33*, 353–360. [CrossRef]

65. Chua, Y.T.; Stair, P.C. An ultraviolet Raman spectroscopic study of coke formation in methanol to hydrocarbons conversion over zeolite H-MFI. *J. Catal.* **2003**, *213*, 39–46. [CrossRef]
66. An, H.; Zhang, F.; Guan, Z.; Liu, X.; Fan, F.; Li, C. Investigating the coke formation mechanism of H-ZSM-5 during methanol dehydration using operando UV-Raman spectroscopy. *ACS Catal.* **2018**, *8*, 9207–9215. [CrossRef]
67. Pala-Rosas, I.; Contreras, J.L.; Salmones, J.; Zeifert, B.; López-Medina, R.; Navarrete-Bolaños, J.; Hernández-Ramírez, S.; Pérez-Cabrera, J.; Fragoso-Montes de Oca, A.A. Catalytic deactivation of HY zeolites in the dehydration of glycerol to acrolein. *Catalysts* **2021**, *11*, 360. [CrossRef]
68. Jiang, X.C.; Zhou, C.H.; Tesser, R.; Di Serio, M.; Tong, D.S.; Zhang, J.R. Coking of catalysts in catalytic glycerol dehydration to acrolein. *Ind. Eng. Chem. Res.* **2018**, *57*, 10736–10753. [CrossRef]
69. Jin, F.; Li, Y. The effect of $H_2$ on Chichibabin condensation catalyzed by pure ZSM-5 and Pt/ZSM-5 for pyridine and 3-picoline synthesis. *Catal. Lett.* **2009**, *131*, 545–551. [CrossRef]
70. Luo, C.W.; Feng, X.Y.; Liu, W.; Lia, X.Y.; Chao, Z.S. Deactivation and regeneration on the ZSM-5-based catalyst for the synthesis of pyridine and 3-picoline. *Microporous Mesoporous Mater.* **2016**, *235*, 261–269. [CrossRef]
71. Jiang, D.; Wang, S.; Li, W.; Xu, L.; Hu, X.; Barati, B.; Zheng, A. Insight into the mechanism of glycerol dehydration and subsequent pyridine synthesis. *ACS Sustain. Chem. Eng.* **2021**, *9*, 3095–3103. [CrossRef]
72. Calvin, J.R.; Davis, R.D.; McAteer, C.H. Mechanistic investigation of the catalyzed vapor-phase formation of pyridine and quinoline bases using $^{13}CH_2O$, $^{13}CH_3OH$, and deuterium-labeled aldehydes. *Appl. Catal. A Gen.* **2005**, *285*, 1–23. [CrossRef]
73. Azaroff, L.V.; Buerger, M.J. *The Powder Method in X-ray Crystallography*; McGraw-Hill: New York, NY, USA, 1958.
74. Emeis, C.A. Determination of Integrated molar extinction coefficients for infrared absorption bands of pyridine adsorbed on solid acid catalysts. *J. Catal.* **1993**, *141*, 347–354. [CrossRef]
75. Brunauer, S.; Emmett, P.H.; Teller, E. Adsorption of gases in multimolecular layers. *J. Am. Chem. Soc.* **1938**, *60*, 309–319. [CrossRef]
76. Barret, E.P.; Joyner, L.G.; Halenda, P.P. The determination of pore volume and area distributions in porous substances. I. Computations from nitrogen isotherms. *J. Am. Chem. Soc.* **1951**, *73*, 373–380. [CrossRef]